Direct Visualization of Order−Order Transitions in Silicon-Containing Block Copolymers by Electron Tomography

Ting-Ya Lo,[†] Rong-Ming Ho,*,[†] Prokopios Georgopanos,[‡] Apostolos Avgeropoulos,[‡] and Takeji Hashimoto[§,⊥]

[†]Department of Chemical Engineering, National Tsing Hua University, Hsinchu 30013, Taiwan, Republic of China
[‡]Department of Materials Science and Engineering, University of Ioannina, University Campus Ioannina 45110, Greece
[§]Quantum Beam Science Directorate, Japan Atomic Energy Agency, Tokai-Mura, Ibaraki Pref. 319-1195, Japan

ⓢ Supporting Information

ABSTRACT: Here, we aim to comprehend the mechanism of the order−order transition (OOT) from nonequilibrium, metastable phase to equilibrium phase. Polystyrene-*block*-polydimethylsiloxane (PS-PDMS) block copolymer (BCP) bulks with metastable cylinder (C) and double gyroid (G) phases can be obtained from lamellae (L) forming PS-PDMS by simply tuning the selectivity of casting solvent. The recovery of the intrinsic L phase can be achieved by thermal annealing through OOT. Time-resolved small-angle X-ray scattering (SAXS) experiments are carried out to reveal the variation of the structural evolution in reciprocal space during annealing. The structural evolution in real space is directly visualized by using electron tomography (i.e., 3D transmission electron microscopy (TEM)). As a result, combining the time-resolved scattering experiments and the morphological observations from electron tomography offers new insights into the phase behaviors of the OOT of BCPs.
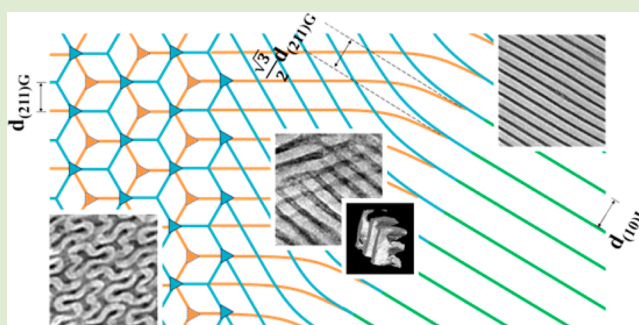
Block copolymers (BCPs) can self-assemble into a variety of ordered nanostructures including spheres (S), hexagonal cylinders (C), gyroid (G), perforated layers (PL), and lamellae (L) through microphase separation for different compositions.[1−3] The phase behavior of self-assembled block copolymers has drawn intensive attention in the past few decades. For practical applications, the self-assembly of BCPs is usually carried out by casting to give the nanostructured phases as bulks or thin films. The self-assembled phases of solution-cast or spin-coated BCP samples depend strongly on the affinity of the solvent between constituent blocks.[4−14] However, the BCP samples casting from solution will usually give nonequilibrium, metastable phases.[15,16] It is noted that the recovery of various metastable phases to thermodynamically stable phases might be reached by thermal annealing at a temperature above the glass transitions of constituted blocks.[15,17−20] Phase transition in self-assembled BCPs between ordered nanostructures is referred to order−order transition (OOT) and has been extensively studied theoretically[21−25] and experimentally.[26−36]

For the exploitation of the nanostructured materials from BCP self-assembly, it is critical to comprehend the mechanism of the OOT from nonequilibrium, metastable phase to equilibrium phase. In most of the experimental studies for the OOT, the structural and morphological evolutions are usually examined by combining small-angle X-ray scattering (SAXS) and transmission electron microscopy (TEM).

However, there is a limitation in the detailed analyses of the transition mechanism because the results acquired from the scattering measurements only provide averaged structural information and it is difficult to give the details of corresponding transition paths. Although TEM has been used as a complementary tool, it is often difficult to elucidate the details of the 3D grains nucleated in the OOT process from 2D projection. To address this problem, electron tomography (i.e., 3D transmission electron microscopy (TEM)) has been developed to directly visualize the self-assembled phases of BCPs in real space.[36−39]

In this study, we aim to examine the phase transition mechanisms of polystyrene-*block*-polydimethylsiloxane (PS-PDMS; 72.5 kg mol^{-1}, PDI ∼ 1.04, f_{PDMS}^v ∼ 0.4) BCP from cylinder to lamellae (C → L) and from gyroid to lamellae (G → L). Owing to the strong segregation of the PS-PDMS, the selectivity of solvent can be exploited for controlling final self-assembled phase after solution casting. Subsequently, metastable C and G phases can be acquired from casting of L-forming PS-PDMS using solvents selectively good for PS. Accordingly, the recovery of metastable phases to thermodynamically stable L phase can be reached by thermal annealing.

Time-resolved small-angle X-ray scattering (SAXS) experiments were carried out to reveal the variation of the structural evolution in reciprocal space during transition. Subsequently, electron tomography was used to directly observe the transition zones of the C → L and the G → L in real space.

As shown in Figure 1a, dark PDMS Cs hexagonally packed in the bright PS matrix can be observed in the as-cast sample from
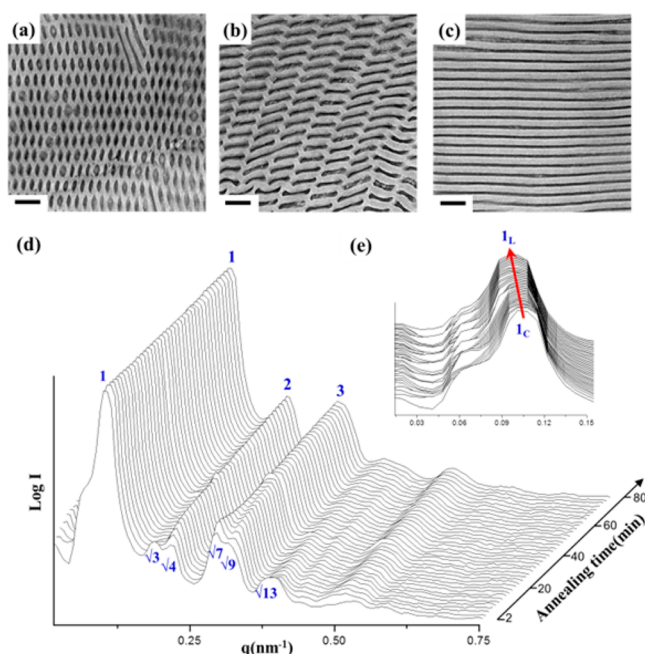

Figure 1. TEM micrographs of as-cast PS-PDMS from chlorobenzene solution without staining (the scale bar is 100 nm): (a) before thermal annealing; (b) after thermal annealing at 160 °C for 1 min; (c) after thermal annealing at 160 °C for 5 min; (d) corresponding time-resolved 1D SAXS profiles were acquired during thermal annealing at 140 °C; and (e) enlarged plot near the primary peak position of $(10)_L$.

chlorobenzene solution. The formation of the metastable C phase is as expected from the selectively good solvent of chlorobenzene for PS at which $\delta_{chlorobenzene} = 9.5$ (cal$^{1/2}$ cm$^{-3/2}$), $\delta_{PS} = 9.1$ (cal$^{1/2}$ cm$^{-3/2}$), and $\delta_{PDMS} = 7.4$ (cal$^{1/2}$ cm$^{-3/2}$). After thermal annealing at 160 °C for 1 min, an interesting dashed-line-like projection image can be found (Figure 1b). With further annealing, as expected from BCP thermodynamics, a typical L morphology is identified (Figure 1c). Also, a series of TEM images at different transition stages of C → L phase transition were acquired (Figure S1).

To further examine the phase-transition behavior, time-resolved SAXS experiments were carried out to reveal the variation of interdomain spacing during transformation. The as-cast samples were thermal annealed at 140 °C to reveal the transition process, and the corresponding SAXS profiles were taken every 2 min. Consistently, the characteristic peaks gradually transform from the reflections of C phase at the relative q values of $\sqrt{3}:\sqrt{4}:\sqrt{7}:\sqrt{9}:(13)^{1/2}$ into the reflections of L phase at the relative q values of 1:2:3 (Figure 1d). There is a consensus that the C → L adopts an epitaxial relationship. Generally, the epitaxial relationship can be justified if the interdomain spacings of $d(10)_L$ and $d(100)_C$ match. By enlarging the profile as shown in Figure 1e, we found that the peak position of $(100)_C$ gradually shifts to the position of $(10)_L$ during transformation. From the SAXS results, the C →

L adopts a well matching of the interdomain spacings of the $(100)_C$ and the $(10)_L$, reflecting a typical type of conventional epitaxial growth.

To truly examine the phase-transition mechanisms of the C → L, electron tomography was carried out to directly visualize the 3D phase morphologies at the transition stages. For the C → L, on the basis of the 2D TEM results, a dashed-line-like projection was found. The curvature change driven by the OOT from C to L may flatten C into a sheet-like shape extended along the $[10]_C$ direction which eventually merges together with neighboring flattened Cs into a short L sheet along the $[10]_C$ direction. On the basis of the reconstructed results (Figure 2), the dashed-line-like image from 2D
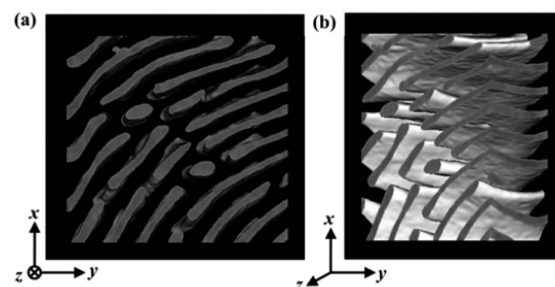
Figure 2. (a) Visualization of the grain boundary between cylinder and lamellae (dashed-line-like texture); (b) tilting of the reconstructed box area of 3D image in (a).

projection is indeed attributed to the cross-section of a 3D ribbon-like L sheet cut with a plane containing its normal vector. Namely, the ribbon-like lamellar sheet is formed by merging the C microdomain along the $[10]_C$ direction of the hexagonal lattice. Eventually, the ribbon-like L sheet will further merge together into L phase with long-range order. Consequently, an epitaxial process by merging the C microdomain directly without any intermediate state is suggested for the C → L.

While the sample was cast from toluene solution, dark tripod-like PDMS microdomains in the bright PS matrix can be observed (Figure 3a). This image corresponds well to the $[111]$ projection of a G phase, attributed to the PS selectivity of toluene ($\delta_{toluene} = 8.9$ (cal$^{1/2}$ cm$^{-3/2}$)) being much lower than that of chlorobenzene in the PS-PDMS. After thermal annealing at 180 °C for 1 min, the images of tripod-like and stripe-like textures can both be found, suggesting the coexistence of G and L phases (Figure 3b). With further annealing, a complete transformation from G to L can be achieved (Figure 3c). Also, a series of TEM images at different transition stages of G → L phase transition were acquired (Figure S2). For time-resolved SAXS experiments, the as-cast samples were thermal annealed at 150 °C, and the corresponding SAXS profiles were taken every 2 min. Consistently, the characteristic peaks indeed gradually transform from the reflections of G phase at the relative q values of $\sqrt{6}:\sqrt{8}:(14)^{1/2}:(22)^{1/2}:(40)^{1/2}:(50)^{1/2}$ into the reflections of L phase at the relative q values of 1:2:3 (Figure 3d). By enlarging the profile, as shown in Figure 3e, interesting results were found at which the primary peak of the G phase (i.e., $(211)_G$) does not gradually shift to the position of the primary peak of the L phase (i.e., $(10)_L$) during transformation. Instead, the peak intensity of $(211)_G$ gradually decreases while the intensity of $(10)_L$ steadily increases. To further examine the shifting of the lattice parameter, the time dependence of the domain
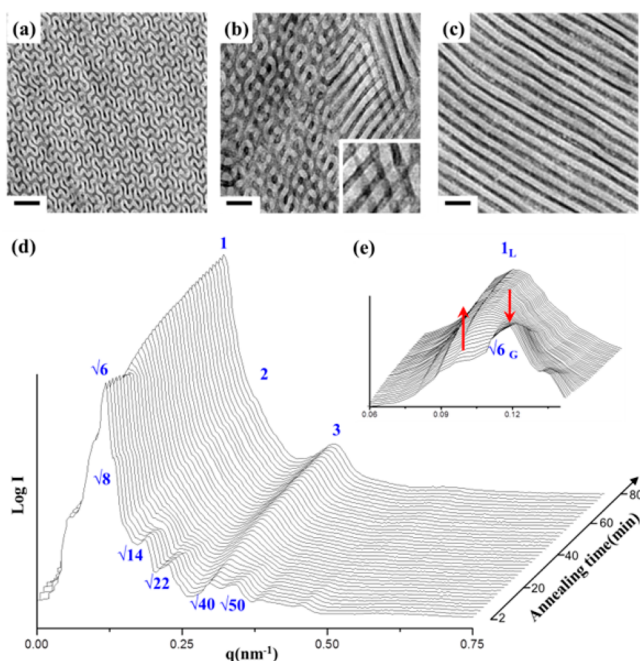
Figure 3. TEM micrographs of as-cast PS-PDMS from toluene solution without staining (the scale bar is 100 nm): (a) before thermal annealing; (b) after thermal annealing at 180 °C for 1 min and the inset shows the enlarged area; (c) after thermal annealing at 180 °C for 5 min; (d) corresponding time-resolved 1D SAXS profiles were acquired during thermal annealing at 150 °C; and (e) enlarged plot near the primary peak position of $(10)_L$.

Figure 4. (a) Visualization of the transitional phase boundary between G and L; (b) enlarged image from the red dashed line box area of 3D image in (a); (c) side view of the reconstructed image of the mesh-like texture; (d) the orthogonal digital slices of reconstructed 3D images (10 nm for the x-y section).

spacings for the C → L and the G → L calculated from time-resolved SAXS results was plotted as shown in Figure S3. Unlike the C → L, a step increasing of domain spacing (approximately 16%) for the G → L can be clearly identified. As a result, we speculate that the phase transition process of the G → L might not be a typical type of conventional epitaxial growth, which suggests that the primary peak of the G phase should gradually shift to the primary peak of the L phase during the epitaxial G → L OOT process.

To further examine the phase transition mechanisms of the G → L, the morphologies at the transition stages were examined by electron tomography to directly visualize the 3D phase images. Note that an interesting mesh-like texture (the inset of Figure 3b) can always be observed in the transition zone of the G → L from 2D TEM projection. We speculate that this unique projection is the specific characteristic of the G → L, reflecting itself the mismatching of interdomain spacings between the G and L phases. Figure 4 displays the reconstructed 3D images of the transition grain viewed along the particular directions, as specified by the Cartesian coordinate attached to each image after binarization and segmentation. On the basis of reconstructed images, it is interesting to recognize that the mesh-like texture is truly a 3D network structure composed of a multiple-layer, lattice-like texture. As shown in Figure 4b,c, a double-layer texture can be clearly identified and the normal directions of these two lattices adopt a specific angle, resulting in the mesh-like projection from 2D TEM. To further examine this interesting mesh-like texture, the digital slices of the x-y section with different z positions were acquired from the reconstructed 3D images. As shown in Figure 4d, the blue one is a left-hand side of the double layer of the image while the red one is the other half of
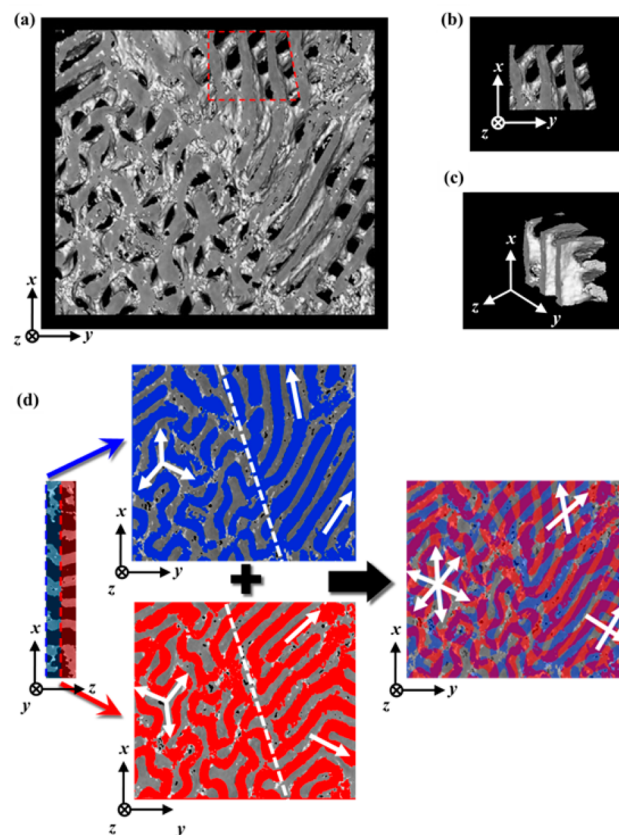
the image. The two x-y sections of the sliced images can be divided into two regions across the white dashed line shown in Figure 4d: the left side (G phase) and the right side (lattice-like phase). On the basis of the x-y sliced images, the tripod orientation of the G phase (on the left side) is different for each layer and the $[10]_L$ direction of the lattice-like phase (on the right side) will follow the direction of one of the arms of the tripod (as marked by the white arrow). As mentioned above, the time-resolved SAXS results suggest that the G → L may not follow the conventional epitaxial growth. However, from the 3D images, the mechanism of the G → L seems to adopt an epitaxial process at which the $(10)_L$ plane will nucleate and grow epitaxially from the $(211)_G$ plane. Most interestingly, the growth directions of these two-layer, lattice-like textures are interdependent from each other. With the decrease of including angle, these two-layer lamellar structures will eventually merge into a unidirectional L phase (Figure S4). Obviously, this mesh-like phase structure may be a consequence of the mismatching of interdomain spacing between the G and L phases as found in the SAXS results.

On the basis of the observations from time-resolved SAXS experiments and electron tomography, the transition mechanisms between the C → L and the G → L were thus proposed. The results indicate interesting geometric rearrangements for the C → L and the G → L. As illustrated in Figure 5a, for the C → L phase transition, the C phase will directly merge along the $[10]_C$ direction to epitaxially transform into a L phase without forming any intermediate transition zone. Those morphological
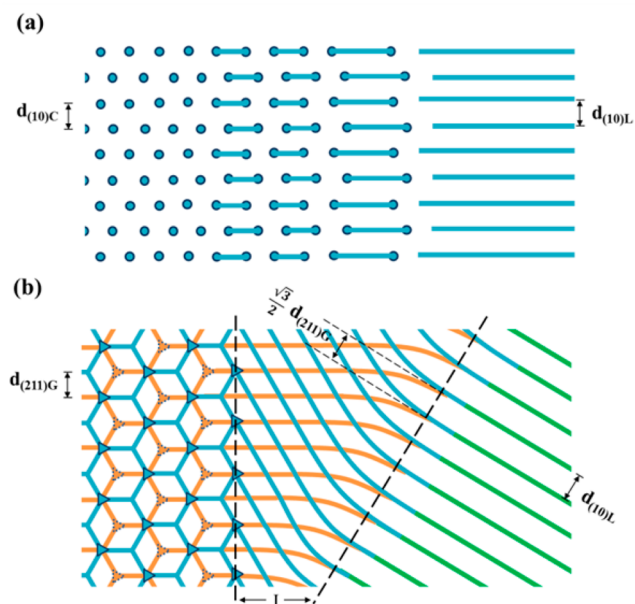
Figure 5. Illustrations of (a) the C → L, the formation of L phase is nucleated from the $(10)_C$ plane, and then those Cs will directly transfer into the $(10)_L$ plane; and (b) the G → L, the formation of L phase is nucleated from the $(211)_G$ plane, and then those Gs will rearrange into diagonal direction of the crisscrossed pattern to form the $(10)_L$ plane.

observations are consistent to the 1D SAXS results exhibiting the matching of interdomain spacing between the C and L phases (i.e., $d(10)_C \sim d(10)_L$). By contrast, for the G → L, the L phase epitaxially grows from the $(211)_G$ plane, through the intermediate mesh-like phase (i.e., lattice-like phase) denoted as I in Figure 5b, where the lattices colored by orange and blue lines grow along the tripod-arm directions and eventually merge into unidirectional lamellae colored by green line in order to reduce the interfacial area, to form the equilibrium L phase. The transition from the I phase to the L phase may involves a decrease of the angle between the lattices within a short distance, hence, the I phase extends over only a short length scale as observed in TEM. Moreover, the large difference between $d(211)_G$ (~52.8 nm) and $d(10)_L$ (~61.0 nm) calculated from the time-resolved SAXS results indicate a significant mismatching (~16%) in the lattices for the G → L, but the mismatching might be quickly accommodated to give the phase transition. From the geometry calculation, $d(10)_L$ corresponding to the length of one of the diagonal lines of the rhombus made out of the orange and blue lines, as indicated in Figure 5b, is equal to $2d(211)_G/\sqrt{3} \sim 61.0$ nm, which is well matched with the spacing of the intrinsic lamellar phase ($d(10)_L \sim 61.0$ nm) calculated from the time-resolved SAXS results. Although the lamellar phase is epitaxially grown from the gyroid phase, the rearrangement of the two-layered structure (indicated by the orange line and the blue line) into the lamellar structure (indicated by green color) in one of the diagonal directions of the rhombus will provide a much more favorable route to adjust the geometric variation in dimension between the G and L phases. Accordingly, the observation of intermediate transition zone between the G and L phases explain the mismatching of interdomain spacing between the G and L phases (i.e., $d(211)_G \neq d(10)_L$). We speculate that the difference between the C → L and the G →

L might be attributed to the difference in structural dimensionality. The L phase is a 1D structure whereas the C phase and the G phases are 2D and 3D structures, respectively. Consequently, for the C → L from 2D to 1D, the variation in the interface curvature can be easily adjusted by merging the cylinders along the $[10]_C$ direction to form the lamellar sheets because the Gaussian curvature is kept zero throughout the OOT from C to L. By contrast, for the G → L from 3D to 1D, an intermediate state to reduce the variation in BCP interface curvature during transition might be required. More specifically, the transition from G to L involves a change of Gaussian curvature from a negative value to zero.

In conclusion, the OOT of the BCP from those metastable phases (C and G phase) to the intrinsic stable phase (L phase) are studied. For the C → L phase transition, the formation of the L phase from the C phase will start from the $(10)_C$ plane and eventually those cylinder will directly merge into a $(10)_L$ plane without passing through any intermediate transition zone. By contrast, for the G → L phase transition, the formation of L from the G phase is nucleated from $(211)_G$ plane, and then the transformation proceeds through an intermediate multiple-layer structure and finally those multiple layer structures will merge to form the $(10)_L$ plane. Accordingly, the transition zone of the multiple-layer structure texture will provide a more favorable route to adjust the geometric variation in dimension between the G and L phases. As a result, combining the morphological observations from time-resolved SAXS and electron tomography offers new insights into BCP phase transitions, and a methodology for systematic studies of the OOT of BCPs is developed.

■ ASSOCIATED CONTENT

Ⓢ Supporting Information

Experimental details. This material is available free of charge via the Internet at http://pubs.acs.org.

■ AUTHOR INFORMATION

Corresponding Authors

*E-mail: rmho@mx.nthu.edu.tw.

[⊥]Professor Emeritus, Kyoto University, Kyoto 606-8501, Japan, and Honorary Char Professor, National Tsing Hua University, Hsinchu, 30013, Taiwan.

Notes

The authors declare no competing financial interest.

■ ACKNOWLEDGMENTS

■ REFERENCES

(1) Bates, F. S.; Fredrickson, G. H. *Annu. Rev. Phys. Chem.* **1990**, *41*, 525.

(2) Matsen, M. W.; Schick, M. *Phys. Rev. Lett.* **1994**, *72*, 2660.

(3) Park, C.; Yoon, J.; Thomas, E. L. *Polymer* **2003**, *44*, 6725.

(4) Hashimoto, T.; Shibayama, M.; Kawai, H. *Macromolecules* **1983**, *16*, 1093.

(5) Balsara, N. P.; Perahia, D.; Safinya, C. R.; Tirrell, M.; Lodge, T. P. *Macromolecules* **1992**, *25*, 3896.

(6) Sakurai, S.; Hashimoto, T.; Fetters, L. J. *Macromolecules* **1996**, *29*, 740.

(7) Hanley, K. J.; Lodge, T. P. *J. Polym. Sci., Polym. Phys. Ed.* **1998**, *36*, 3101.

(8) Wanka, G.; Hoffmann, H.; Ulbricht, W. *Macromolecules* **1994**, *27*, 4145.

(9) Almgren, M.; Brown, W.; Hvidt, S. *Colloid Polym. Sci.* **1995**, *273*, 2.

(10) Hajduk, D. A.; Kossuth, M. B.; Hillmyer, M. A.; Bates, F. S. *J. Phys. Chem. B* **1998**, *102*, 4269.

(11) Hanley, K. J.; Lodge, T. P.; Huang, C.-I. *Macromolecules* **2000**, *33*, 5918.

(12) Lai, C.; Russel, W. B.; Register, R. A. *Macromolecules* **2002**, *35*, 841.

(13) Inoue, T.; Soen, T.; Hashimoto, T.; Kawai, H. *J. Polym. Sci., Part A: Polym. chem.* **1969**, *7*, 1283.

(14) Mori, K.; Hasegawa, H.; Hashimoto, T. *Polymer* **1990**, *31*, 2368.

(15) Sakurai, S.; Umeda, H.; Taie, K.; Nomura, S. *J. Chem. Phys.* **1996**, *105*, 8902.

(16) Hajduk, D. A.; Gruner, S. M.; Rangarajan, P.; Register, R. A.; Fetters, L. J.; Honeker, C.; Albalak, R. J.; Thomas, E. L. *Macromolecules* **1994**, *27*, 490.

(17) Thomas, E. L.; Alward, D. B.; Kinning, D. J.; Martin, D. C.; Handlin, D. L.; Fetters, L. J. *Macromolecules* **1986**, *19*, 2197.

(18) Sakurai, S.; Momii, T.; Taie, K.; Shibayama, M.; Nomura, S.; Hashimoto, T. *Macromolecules* **1993**, *26*, 485.

(19) Jeong, U.; Lee, H. H.; Yang, H.; Kim, J. K.; Okamoto, S.; Aida, S.; Sakurai, S. *Macromolecules* **2003**, *36*, 1685.

(20) Cohen, R. E.; Bates, F. S. *J. Polym. Sci., Polym. Phys. Ed.* **1980**, *18*, 2143.

(21) Matsen, M. W.; Schick, M. *Phys. Rev. Lett.* **1994**, *72*, 2660.

(22) Matsen, M. W. *Phys. Rev. Lett.* **1998**, *80*, 4470.

(23) Laradji, M.; Shi, A.-C.; Desai, R. C.; Noolandi, J. *Phys. Rev. Lett.* **1997**, *78*, 2588.

(24) Qi, S.; Wang, Z.-G. *Phys. Rev. Lett.* **1996**, *76*, 1679.

(25) Yu, B.; Li, B.; Sun, P.; Chen, T.; Jin, Q.; Ding, D.; Shi, A. C. *J. Chem. Phys.* **2005**, *123*, 234902.

(26) Khandpur, A. K.; Förster, S.; Bates, F. S.; Hamley, I. W.; Ryan, A. J.; Bras, W.; Almdal, K.; Mortensen, K. *Macromolecules* **1995**, *28*, 8796.

(27) Hajduk, D. A.; Takenouchi, H.; Hillmyer, M. A.; Bates, F. S.; Vigild, M. E.; Almdal, K. *Macromolecules* **1997**, *30*, 3788.

(28) Kim, J. K.; Lee, H. H.; Gu, Q.; Chang, T.; Jeong, Y. H. *Macromolecules* **1998**, *31*, 4045.

(29) Ryu, C. Y.; Lee, M. S.; Hajduk, D. A.; Lodge, T. P. *J. Polym. Sci., Polym. Phys. Ed.* **1997**, *35*, 2811.

(30) Floudas, G.; Ulrich, R.; Wiesner, U. *J. Chem. Phys.* **1999**, *110*, 652.

(31) Hajduk, D. A.; Gruner, S. M.; Rangarajan, P.; Register, R. A.; Fetters, L. J.; Honeker, C.; Albalak, R. J.; Thomas, E. L. *Macromolecules* **1994**, *27*, 490.

(32) Wang, C.-Y.; Lodge, T. P. *Macromol. Rapid Commun.* **2002**, *23*, 49.

(33) Schulz, M. F.; Bates, F. S.; Almdal, K.; Mortensen, K. *Phys. Rev. Lett.* **1994**, *73*, 86.

(34) Hajduk, D. A.; Ho, R. M.; Hillmyer, M. A.; Bates, F. S.; Almdal, K. *J. Phys. Chem., Part B: Polym. Phys.* **1998**, *102*, 1356.

(35) Jinnai, H.; Hasegawa, H.; Nishikawa, Y.; Sevink, G. J. A.; Braunfeld, M. B.; Agard, D. A.; Spontak, R. J. *Macromol. Rapid Commun.* **2006**, *27*, 1424.

(36) Chen, C. K.; Hsueh, H. Y.; Chiang, Y. W.; Ho, R. M.; Akasaka, S.; Hasegawa, H. *Macromolecules* **2010**, *43*, 8637.

(37) Yamauchi, K.; Takahashi, K.; Hasegawa, H.; Iatrou, H.; Hadjichristidis, N.; Kaneko, T.; Nishikawa, Y.; Jinnai, H.; Matsui, T.; Nishioka, H.; Shimizu, M.; Furukawa, H. *Macromolecules* **2003**, *36*, 6962.

(38) Jung, J.; Park, H. W.; Lee, S.; Lee, H.; Chang, T.; Matsunaga, K.; Jinnai, H. *ACS Nano* **2010**, *4*, 3109.

(39) Mareau, V. H.; Akasaka, S.; Osaka, T.; Hasegawa, H. *Macromolecules* **2007**, *40*, 9032.